Modeling of Micro- and Macrosegregation and Freckle Formation in Single-Crystal Nickel-Base Superalloy Directional Solidification

M.C. SCHNEIDER, J.P. GU, C. BECKERMANN, W.J. BOETTINGER, and U.R. KATTNER

The formation of macrosegregation and freckles by multicomponent thermosolutal convection during the directional solidification of single-crystal Ni-base superalloys is numerically simulated. The model links a previously developed thermodynamic phase equilibrium subroutine with an existing code for simultaneously solving the macroscopic mass, momentum, energy, and species conservation equations for solidification of a multicomponent alloy. Simulation results are presented for a variety of casting speeds and imposed thermal gradients and for two alloy compositions. It is found that for a given alloy composition, the onset of convection and freckle formation occurs at a critical primary dendrite arm spacing, which agrees well with previous experimental findings. The predicted number and shape of the freckle chains in the unstable cases also agree qualitatively with experimental observations. Finally, it is demonstrated how the onset and nature of convection and macrosegregation vary with alloy composition. It is concluded that the present model can provide a valuable tool in predicting freckle defects in directional solidification of Ni-base superalloys.

I. INTRODUCTION

THE formation of freckles (or channel segregates) and macrosegregation in directional solidification of Ni-base superalloys has been the subject of numerous studies since the pioneering work of Giamei and Kear.[1] Copley *et al.*[2] suggested a criterion for freckle formation in steady columnar growth that is based on a critical cooling rate, $\dot{T}$ (*i.e.*, the product of imposed casting speed, R, and temperature gradient, G), below which freckles are likely to form (if G is below a certain critical value). Experiments on transparent model alloys and binary metallic alloys have shown that freckles are initiated by convective instabilities above or in the mushy zone (for example, References 3 through 5). Instabilities can develop in a positive thermal gradient when the segregated interdendritic liquid is less dense than the overlying bulk liquid of original composition. In the unstable mode, low-density liquid emanates from the mushy zone in the form of solutal plumes, or fingers, which are fed by flow of segregated liquid through the surrounding mush. This flow causes delayed growth and even remelting of dendrites, leading to the formation of a narrow, open channel in the mushy zone below each plume. The channel thus provides a self-sustaining path for feeding the plume. The channels eventually freeze and appear as chains of equiaxed grains (*i.e.*, freckles) in the solidified superalloy.

In the 1990s, there has been renewed interest in the ability to predict the formation of freckles and other defects in single-crystal, investment-cast Ni-base superalloys.[6–11] For example, in the most recent study by Pollock and Murphy,[11] detailed experiments were performed that indicate a strong correlation between the primary dendrite arm spacing and freckle formation for various SX alloys. For one alloy, the critical primary dendrite arm spacing was found to be 320 μm. The primary dendrite arm spacing, in turn, correlates well with the cooling rate (as subsequently discussed), thus confirming the criterion by Copley *et al.*[2] Another relationship, where λ_1 is proportional to $G^{-1/2} \times R^{-1/4}$, produced a similar or slightly better criterion for freckle formation.[11] It was noted that accurate predictions using numerical models are still not possible, primarily due to the complex thermosolutal convection patterns. Clearly, such modeling requires an understanding of the complicated solute partitioning behavior during solidification of superalloys and its effect on liquid density, as well as a consideration of the influence of dendrite morphology on melt flow in the mushy zone. To date, all reported simulations of investment casting of multicomponent superalloys have considered heat conduction only (other than for mold filling).

Macrosegregation in alloy solidification was first modeled by Flemings and Nereo.[12] More recently, numerous studies have demonstrated the ability of fully coupled solidification and convection models to numerically predict freckles in directional solidification of binary alloys (for example, References 13 through 15). Stability analyses also have been performed for directional solidification of binary alloys with a mushy zone (for example, References 16 through 18). Although these studies have provided much insight, they are difficult to apply directly to the prediction of freckles in multicomponent superalloys. Multicomponent models that couple mass, momentum, energy, and species conservation equations in all regions (solid, mush, and liquid) have recently been developed for steel solidification.[19–23] In particular, Schneider and Beckermann[23] used constant liquidus slopes and partition coefficients for a ten-element steel and were able to predict the formation of A segregates—a macrosegregation pattern closely related to freckles.

M.C. SCHNEIDER, formerly Graduate Research Assistant, Department of Mechanical Engineering, University of Iowa, is with Software Development, Magma GmbH, Aachen, Germany, 52072. J.P. GU, Postdoctoral Researcher, and C. BECKERMANN, Professor, are with the Department of Mechanical Engineering, The University of Iowa, Iowa City, IA 52242-1527. W.J. BOETTINGER and U.R. KATTNER, Metallurgists, are with the Metallurgy Division, NIST, Gaithersburg, MD 20899.

Manuscript submitted October 28, 1996.

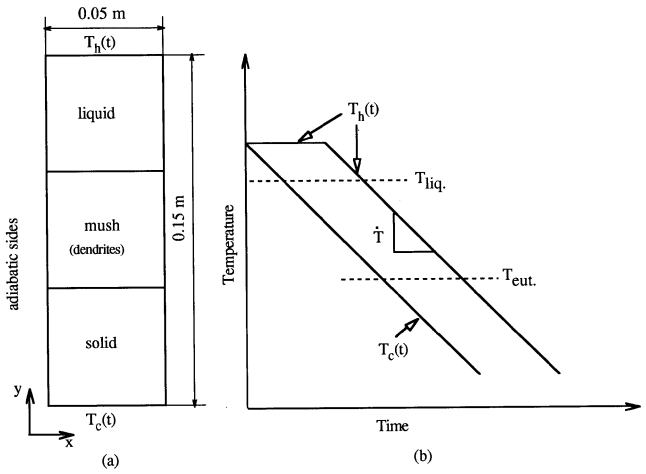

Fig. 1—Simulation conditions: (*a*) geometry and boundary conditions and (*b*) variation of hot top and cold bottom wall temperatures.

One outcome of the study on steel solidification[23] was the finding that the realistic prediction of macrosegregation in multicomponent alloys requires accurate models of phase equilibrium, solidification path, and microsegregation. Despite the common use of Ni-base superalloys, relatively little is known about such issues. Most information is available for INCONEL*-type alloys, for which more detailed analyses have been performed.[24–32] Boettinger *et al.*[32] directly employed multicomponent thermodynamic calculations of the phase boundaries between liquid and various solid phases in solving microscopic solute conservation equations for a one-dimensional (1-D), platelike dendrite arm geometry. This approach naturally treats the temperature and/or concentration dependence of partition coefficients and liquidus slopes, and the formation of secondary phases. In addition, the same database can be used for Ni-base superalloys of different compositions. It is cautioned, however, that the thermodynamic database used in the equilibrium calculations of Reference 32 is quite simple. More refined databases can be used in future calculations, and the reader is referred to Reference 33 for further discussion.

*INCONEL is a trademark of INCO Alloys International, Inc., Huntington, WV.

The objective of this present study is twofold. From a basic modeling perspective, the goal is to link the thermodynamic phase equilibrium subroutine of Boettinger *et al.*,[32] to the multicomponent solidification with convection code of Schneider and Beckermann[23] to create a model for calculating macrosegregation in Ni-base superalloys. This combined model is then used to investigate the occurrence and the nature of freckle formation in directional solidification in a two-dimensional (2-D) rectangular geometry.

II. MODEL DESCRIPTION

The system and boundary conditions analyzed in the present study are shown in Figure 1. The alloy is contained in a rectangular cavity of height and width equal to 0.15 and 0.05 m, respectively. The vertical sidewalls are adiabatic, while the top and bottom walls are maintained at time-varying hot and cold temperatures, respectively. This configuration is thought to mimic an idealized directional solidification process. The casting conditions are specified through the choice of an average temperature gradient, $G = (T_h - T_c)/H$, and a casting speed, R, so that the mean cooling rate, $\dot{T}$, is given by

$$\dot{T} = GR \qquad [1]$$

The parameters G and R are then used to determine the variation of the hot and cold wall temperatures, as shown in Figure 1(b). In all simulations, the melt is initially quiescent with a uniform composition and temperature of 150 K above the liquidus temperature. A no-slip velocity condition is used on all boundaries.

The governing macroscopic conservation equations for mass, momentum, energy, and species are identical to those in Table I of Reference 23 and are not repeated here. The solid phase is assumed to be stationary and rigid and in local thermal equilibrium with the liquid in the mush. Separate species conservation equations are solved for each element in both the liquid and solid phases. The liquid within a small-volume element in the mush is assumed to be solutally well mixed, so that the volume-averaged liquid concentration for each species is equal to the interfacial value as given by phase equilibrium. The macroscopic solid species conservation equations incorporate a back-diffusion model to account for microsegregation.[23,34] This back-diffusion model is based on the assumption of a 1-D platelike dendrite arm geometry and parabolic concentration profiles locally in the solid. The performance of the back-diffusion model for Ni-base superalloys is examined in the next section. All cross-diffusion terms are neglected. Liquid melt motion is driven by thermosolutal buoyancy forces, contraction-driven flow is neglected, and the liquid drag in the mush is modeled using a permeability (as subsequently discussed). Other explanations can be found in the original reference.[23] Subsequently discussed in detail are those aspects of the model that are unique to the present simulations of directional solidification of Ni-base superalloys.

A. *Phase Equilibrium and Solid Microsegregation*

A major emphasis in the present study has been the integration of an available phase equilibrium subroutine for Ni-base superalloys[32] into the solidification simulations. The phase equilibrium subroutine developed by Boettinger *et al.*[32] is based on the CALPHAD method[35] and relies on the use of thermodynamic free energy functions for the relevant phases in the alloy. The subroutine accepts the liquid concentrations, C_l^m, as input and calculates the corresponding equilibrium liquidus temperature, T; the interfacial solid concentrations, C_{sl}^m; and the liquidus slopes, $m^m = \partial T/\partial C_l^m$, where the superscript m indicates the species. Thus, the subroutine establishes the relation

$$C_l^m \Rightarrow (T, C_{sl}^m, m^m) \qquad [2]$$

Note that the partition coefficients, κ^m, are equal to C_{sl}^m/C_l^m. The thermodynamic database for ten-component Ni-base superalloys consists of coefficients for polynomials that are used to describe the free energies of the individual phases as functions of temperature and composition. The database is considered to be preliminary because it consists only of

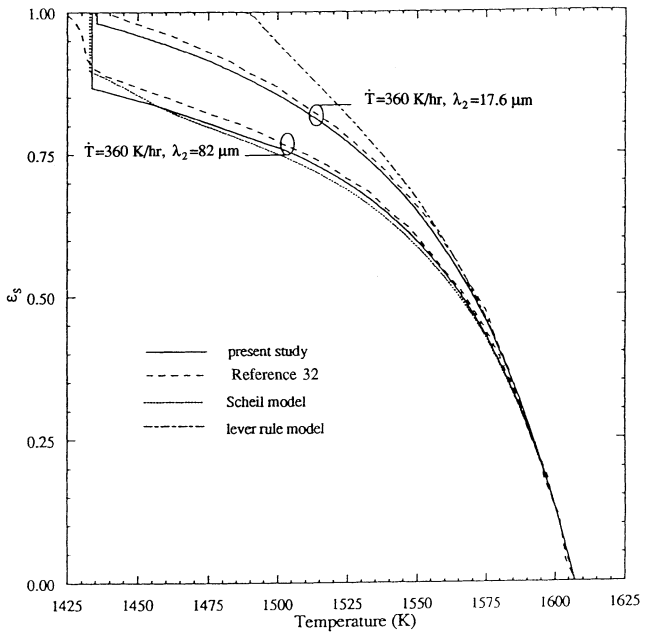

(a)

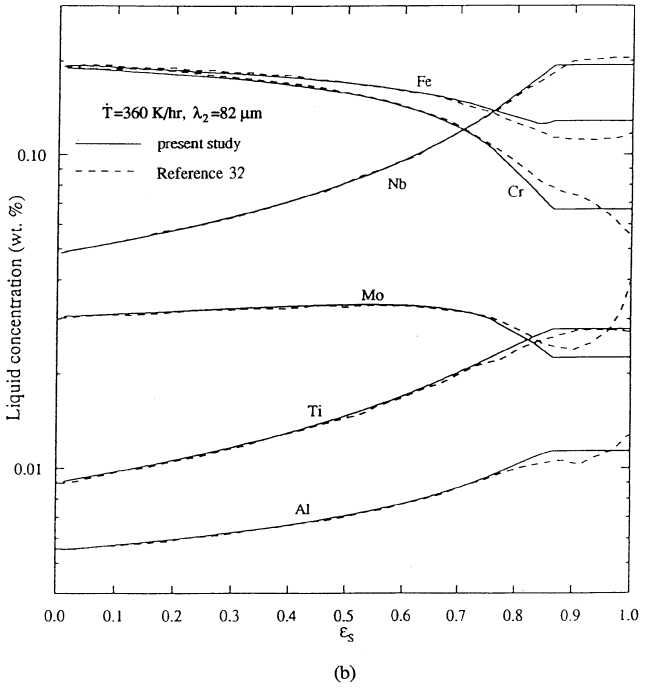

(b)

Fig. 2—Comparison of the present microsegregation calculation using the approximate back-diffusion model with the results of Boettinger *et al.*[32] for IN718: (*a*) comparison of the evolution of solid fraction with temperature and (*b*) comparison of the change in liquid composition with solid fraction.

coefficients for the corresponding binary alloy systems, with an extrapolation procedure used for higher order systems. In addition, the presence of carbon is ignored so that the formation of niobium carbide cannot be predicted, and the thermodynamic model for the Laves phase (which forms during the eutectic reaction) was constructed using the free energies of stable and metastable binary Laves phases. All other details can be found in the original reference.[32]

In this work, the phase equilibrium subroutine was coupled with the solidification model and used to calculate the two-phase equilibrium between the liquid and the primary γ-solid phases only. Because three-phase equilibrium calculations were not considered here, solidification was assumed to conclude *via* an isothermal eutectic reaction.

In order to validate the present implementation and back-diffusion model, simulations were first performed for the limiting case of solidification of a small-volume element at a uniform temperature (no flow) cooled at a constant rate. A comparison to the results of Boettinger *et al.*[32] for an alloy similar to IN718* (52Ni, 19.0Cr, 0.25Co, 0.90Ti, 0.020Ta, 0.55Al, 3.05Mo, 4.85Nb, and 19.4Fe, by wt pct) was made. Perfect agreement was achieved for standard Scheil and Lever analyses. In the back-diffusion analysis, Boettinger *et al.* numerically solved the 1-D (for a plate dendrite) diffusion equation in the solid, coupled with overall solute balances in the solid and well-mixed liquid. Arrhenius relations were used to account for the temperature dependence of the solid mass diffusivities.

*IN718 is a trademark of INCO Alloys International, Inc., Huntington, WV.

Figure 2 shows a comparison of the present microsegregation calculation using the approximate back-diffusion model[23,34] with the ''exact'' results of Boettinger *et al.*[32] The curves for the evolution of the solid fraction with temperature (Figure 2(a)) are in good agreement for both of the assumed dendrite arm spacings[32] and a cooling rate of 360 K/h. The difference at very high solid fractions can be attributed to the simplified treatment of the eutectic reaction in the present study. The curves for the change in the liquid concentrations with solid fraction (Figure 2(b)) show similar agreement. Note that the Fe and Cr contents of the liquid decrease during solidification due to their preferential incorporation into the solid, while the Nb, Ti, and Al liquid concentrations increase due to their rejection from the solid. Molybdenum is initially rejected from the solid, but at solid fractions greater than about 0.6 it becomes preferentially incorporated, indicating a change in the partition coefficient from less than to greater than unity. The differences during the formation of the Laves phase at high solid fraction are expected to have a negligible influence on the flow and macrosegregation predictions of the present study.

The following directional solidification simulations are made for a CMSX2 alloy, whose composition and other properties are listed in Table I, as well as for a modified CMSX2 alloy, where Ta was decreased from 6 to 1 pct, and W was increased from 8 to 13 pct. The calculated liquidus temperatures are 1606 and 1628 K, respectively, for the original and modified compositions. The eutectic cutoff temperatures are 1486 and 1533 K for the two alloys, which correspond to the point where finite-rate back-diffusion calculations (with a cooling rate of 360 K/h and a dendrite arm spacing of 90 μm) gave a solid fraction of 0.9. This procedure can only be viewed as a compromise between having too large an amount of eutectic solid and having too large a solidification temperature range. Improvements will be possible when the three-phase equilibrium calculations are performed.

Table I. Aim Composition for the CMSX2 Alloy; Equilibrium Solid Composition, Liquidus Slopes, and Partition Coefficients Evaluated at Liquidus Temperature (1606 K); Solutal Expansion Coefficients for Each of the Elements; and Coefficients for Calculation of Solid Diffusion Coefficient of Each Element in Ni Using the Arrhenius-Type Relationship $D_s^m = D_{so}^m \exp\{-Q/\bar{R}T\}$

Element	C_{in}^m (wt pct)	C_{sl}^m (wt pct)	m^m (K/wt pct)	κ^m (wt pct/wt pct)	β_C^m (1/wt pct)*	D_{so}^m (m^2 / s)**	Q (J/mole)**
Ni	65.8	68.2	—	—	—	—	—
Cr	8.0	8.45	−1.80	1.06	1.9×10^{-3}	5.0×10^{-5}	260×10^3
Co	5.0	3.49	−5.73	0.699	1.3×10^{-4}	2.2×10^{-5}	256.2×10^3
Ti	1.0	0.492	−16.3	0.492	8.2×10^{-3}	8.6×10^{-5}	257.1×10^3
Ta	6.0	3.27	−5.00	0.545	-4.6×10^{-3}	9.0×10^{-5}	278.7×10^3
Al	5.6	5.11	−15.44	0.913	2.5×10^{-2}	1.9×10^{-4}	268×10^3
Mo	0.6	0.403	−5.72	0.672	-1.8×10^{-3}	3.0×10^{-4}	288.5×10^3
W	8.0	10.6	−0.641	1.32	-5.3×10^{-3}	8.6×10^{-5}	294.8×10^3

*From Ref. 36.
**From Ref. 32.

Table II. Thermophysical Properties, Dendrite Arm Spacing Relation, and Mushy Zone Permeability Relation Used in the Directional Solidification Simulations

Density* $\rho_s = \rho_{ref} = 8100$ kg/m^3	Thermal expansion coefficient** $\beta_T = 1.4 \times 10^{-4}$ K^{-1}
Solid specific heat* $c_s = 630$ J/kg/K	Liquid specific heat* $c_l = 700$ J/kg/K
Latent heat* $L = 185 \times 10^3$ J/kg	Liquid viscosity* $\mu_l = 6.9 \times 10^{-3}$ kg/m/s
Solid thermal conductivity* $k_s = 27$ W/m/K	Liquid thermal conductivity* $k_l = 34$ W/m/K
	Liquid diffusion coefficient (assumed) $D_l^m = 3.6 \times 10^{-9}$ m^2/s
Mushy zone permeability $K = K_0 \frac{\varepsilon_l^3}{(1-\varepsilon_l)^2}$ where $K_0 = 6 \times 10^{-4}\ \lambda_1^2$	Primary dendrite arm spacing† $\log \lambda_1 = -0.3384 \log \dot{T} + 2.166$ where $\dot{T}$ is the cooling rate in K/s and λ_1 is in micrometers

*From Ref. 40.
**From Refs. 36.
†Deduced from Ref. 38 and 39.

B. *Properties and Supplementary Relations*

All thermophysical properties used in the present simulations are summarized in Tables I and II. Note that the solid composition, liquidus slopes, and partition coefficients given in Table I were evaluated at the liquidus temperature using the phase equilibrium subroutine and do vary as discussed in Section A. Of particular importance in the present simulations are the thermal and solutal expansion coefficients used to calculate the liquid density in the buoyancy term in the momentum equations. The solute coefficients in Table I were determined by weighting the liquid molar volumes of the individual elements (as linear functions of temperature) with their initial mole fractions, according to the procedure in Iida and Guthrie.[36] For illustration purposes, Figures 3(a) and (b) show the variation of the liquid density of the CMSX2 alloy during solidification. For simplicity, the solidification path was calculated according to the Scheil model. The relative density change plotted in Figure 3 is proportional to the buoyancy force in the mushy zone (Eq. [12] in Reference 23). It can be seen that for the vertically upward directional solidification simulations of the present study, the total buoyancy force is generally destabilizing, that is, the density decreases with increasing solid fraction (i.e., at lower temperatures in the downward direction). The ratio of the thermal to solutal buoyancy forces is negative and less than unity (Figure 3(a)), indicating that, while the thermal buoyancy is stabilizing, the solutal buoyancy is stronger and destabilizing during solidification of the CMSX2 alloy. The individual contributions of the various elements to the total density variation are shown in Figure 3(b). Tantalum (Ta) makes the strongest stabilizing influence on the buoyancy force, whereas W and Al are most destabilizing. The elements Mo, Cr, and Co are relatively neutral. In order to investigate the effects of an even more unstable density profile in the directional solidification simulations, the modified CMSX2 alloy was chosen to have decreased Ta and increased W contents (refer to Section A). The resulting buoyancy forces are roughly four times more destabilizing than for the original CMSX2 alloy.

Of critical importance to the onset and extent of convection in the present simulations is the relation used to calculate the local permeability of the mushy zone as a function of the liquid volume fraction and the primary dendrite arm spacing, λ_1. The relation given in Table II is based on the isotropic Blake–Kozeny equation. The permeability is proportional to λ_1^2, implying that a lower arm spacing leads to lower permeability and, hence, a higher resistance to flow in the mush. The numerical value of the constant K_0 was obtained from a best fit of all experimental (at intermediate liquid fractions) and simulated (at high liquid fractions) permeability data for flow parallel and perpendicular to primary dendrite arms, as summarized in the thesis of Bhat.[37] The resulting curve fit is shown in Figure 4. The primary dendrite arm spacing generally decreases with increasing cooling rate ($\dot{T}$), and it is crucial to take this effect into account in the permeability. The relatively simple relationship between λ_1 and $\dot{T}$ given in Table II was found to be applicable to a wide range of directionally solidified superalloys,[38,39] although more complicated relations also work well.[11]

III. NUMERICAL PROCEDURE

The numerical procedures used to solve the governing conservation equations are identical to those in Reference 23 and involve a fixed-grid, single-domain, implicit, finite-volume scheme. The coupling of the energy and spe-

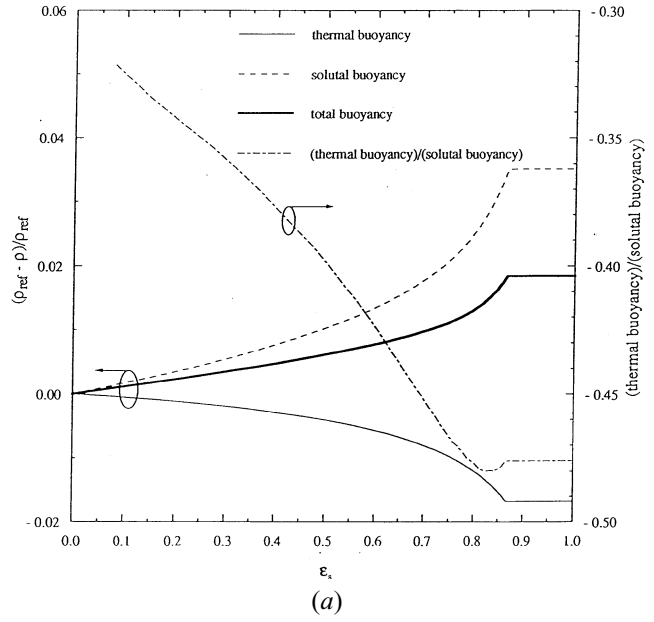

(*a*)

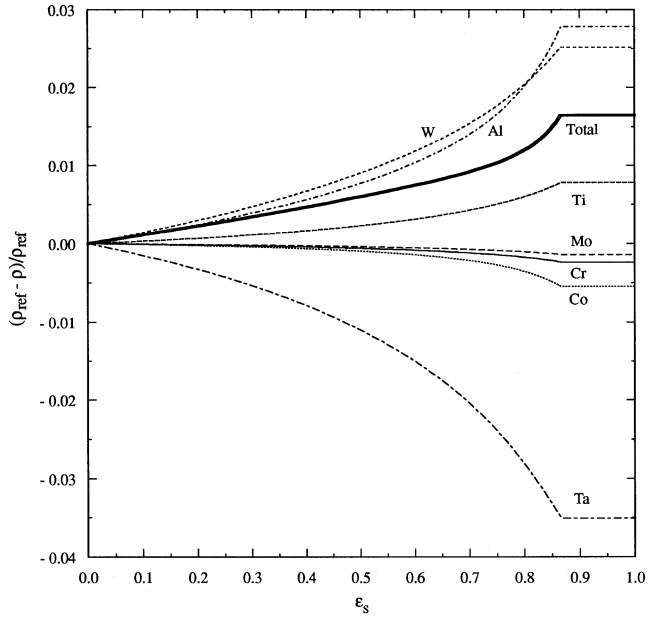

(*b*)

Fig. 3—Variation of the liquid density of the CMSX2 alloy during solidification (Scheil model): (*a*) change of thermal, solutal, and total buoyancy with solid fraction; and (*b*) contribution of each element to the variation of the liquid density.

cies conservation equations in the mushy zone through phase equilibrium provides a method for calculating the solid volume fraction.[41] The procedure used is similar to the one described in Reference 23, with some modifications necessary to accommodate the use of the phase equilibrium subroutine instead of having an explicit relation between liquidus temperature and concentrations. Essentially, it involves linearization of the liquidus slopes over a time-step together with Newton–Raphson iteration.[41] Calculating thermodynamic equilibrium conditions for each control volume at every iteration during each time-step would lead to unrealistically long computational times. Therefore, for the results presented in the following section, the equilibrium subroutine was called only at the beginning of every second

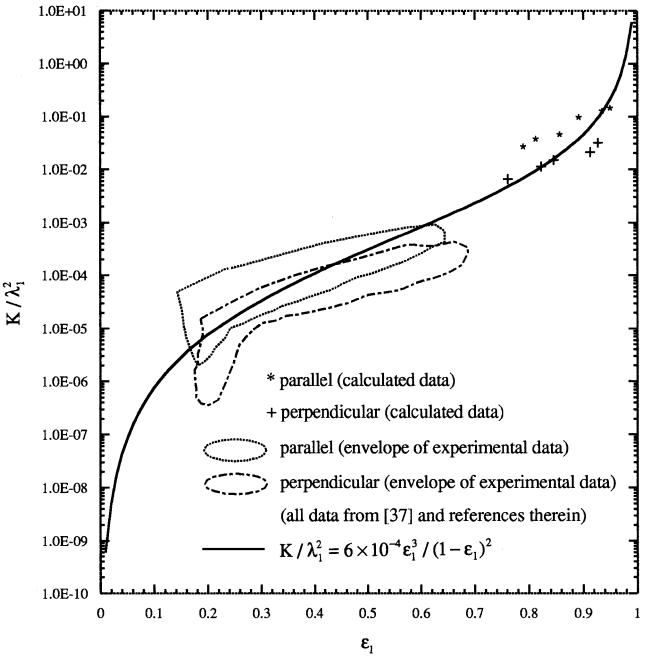

Fig. 4—Variation of the dimensionless permeability with liquid fraction and comparison with measured and predicted permeability data for flow parallel and perpendicular to the primary dendrite arms.

time-step. Simulations without flow showed that this simplification led to differences of less than 1 pct in the predicted temperatures and concentrations. Even with this reduction in calls to the equilibrium subroutine, the phase equilibrium calculations consumed up to 50 pct of the total computational time.

The computations were performed on a uniform grid that had 50 and 75 control volumes (*i.e.*, 1 × 2 mm in actual size) in the horizontal and vertical directions, respectively. A time-step of 0.5 seconds was used in obtaining most results. Considerable effort was made to assure that the solution procedures are sound. The grid and time-step are fine enough to capture all of the fundamental transport phenomena while allowing for reasonable computational costs. It was found that a coarser grid would not allow for the prediction of any channel segregates. Simulation of a solidification time of 1 second of the eight-element CMSX2 alloy required approximately 300 seconds of CPU time on a single processor of a SGI Power Challenge, XL-16. Hence, a typical simulation lasting 6000 seconds required three CPU-weeks.

IV. RESULTS AND DISCUSSION

In order to investigate the effects of casting parameters and alloy composition on the stability of convection and the formation of macrosegregation in the present system, a total of six simulations have been performed. The conditions are summarized in Table III. Cases 1 through 4 correspond to the CMSX2 alloy of the original composition and illustrate the influence of cooling rate by varying the mean temperature gradient and casting speed. Cases 1m and 4m are equivalent to Cases 1 and 4, respectively, except that the alloy composition corresponds to the more unstable, modified CMSX2 alloy (Ta decreased from 6 to 1 pct, W increased from 8 to 13 pct).

Table III. Summary of Simulation Cases

Case	Alloy	G (K/cm)	R (cm/h)	$\dot{T}$ (K/h)	λ_1 (μm)	Result
1	original CMSX2	50	25	1250	210	stable
2	original CMSX2	35	10	350	320	just unstable
3	original CMSX2	30	10	300	340	unstable
4	original CMSX2	20	10	200	400	unstable
1m	modified CMSX2	50	25	1250	210	just unstable
4m	modified CMSX2	20	10	200	400	unstable

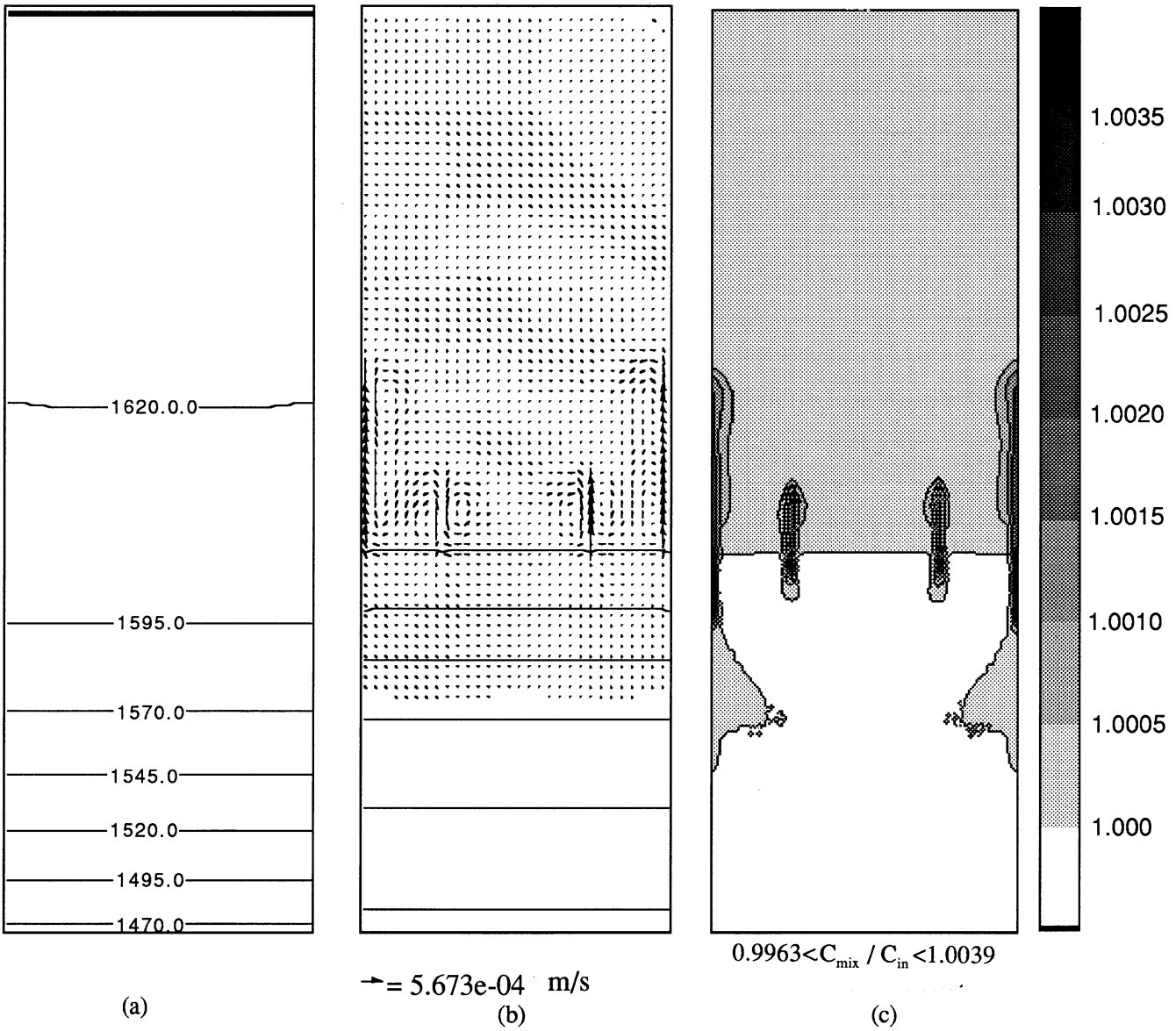

Fig. 5—Case 2 at 2971 s: (*a*) isotherms in Kelvin, (*b*) velocity vectors and solid fraction contours (increasing in 20 pct increments from top), and (*c*) normalized mixture concentration pattern of Ti.

In the following plots, the velocity vectors represent the intrinsic volume averaged (not superficial) liquid velocity, and a velocity scale is provided at the bottom of each plot. The velocity vectors are interpolated on a coarser grid for better visualization. Superimposed on the vector plots are solid volume fraction contours in 20 pct increments. The shaded macrosegregation plots are of the mixture concentration ($C_{\text{mix}} = \varepsilon_l C_l^m + \varepsilon_s C_s^m$) normalized by the initial concentration, C_{in}, of the element under consideration. Space limitations prohibit the presentation of concentration plots for all of the elements in the multicomponent alloy, and only one of the elements (*i.e.*, Ti) is chosen. It is shown in Reference 23 that the normalized mixture concentration plots for all elements (in steel) look similar if scaled by the partition coefficient of an element. However, some local differences in the macrosegregation patterns are possible.[23]

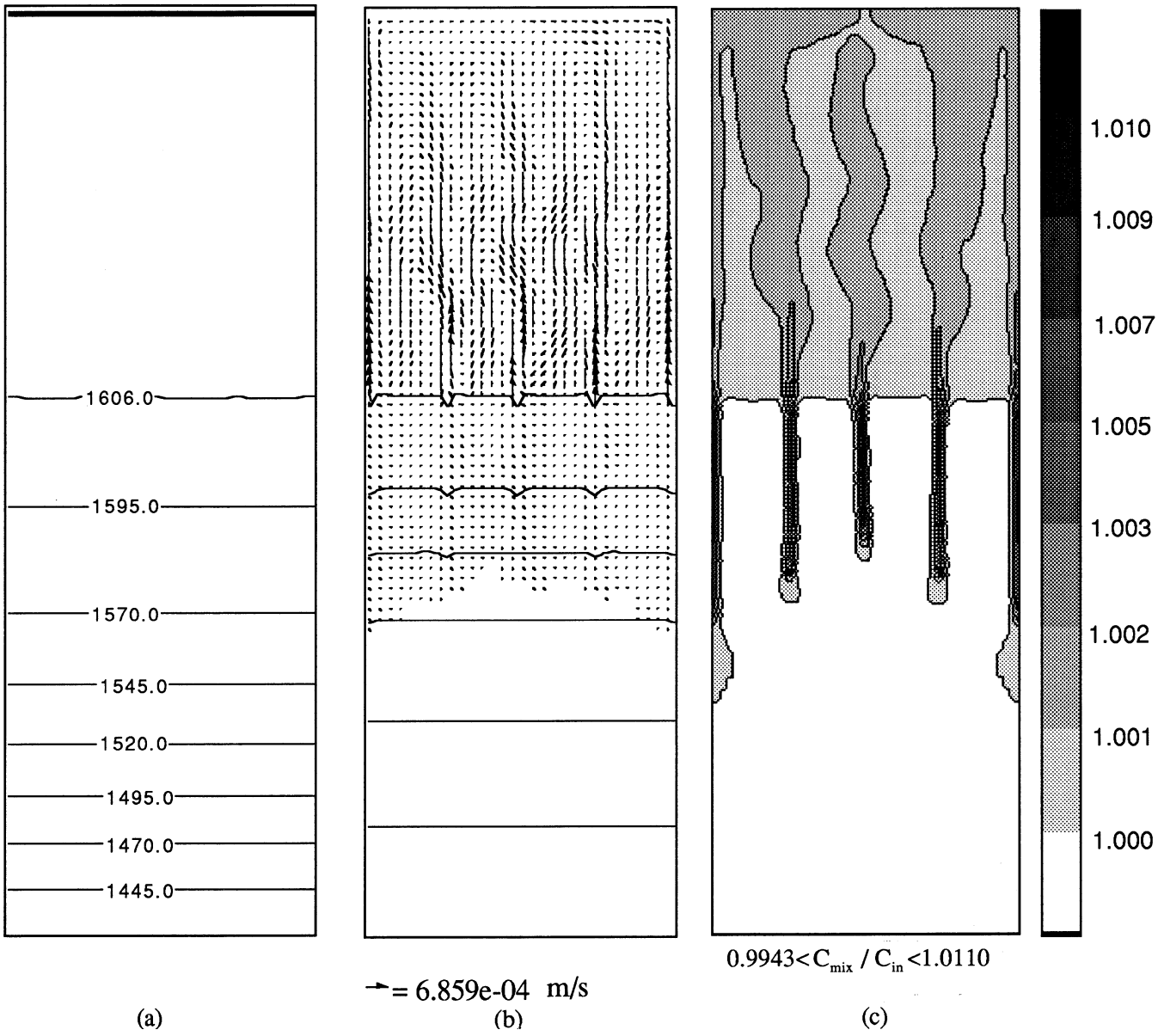

Fig. 6—Case 2 at 3451s: (*a*) isotherms in Kelvin, (*b*) velocity vectors and solid fraction contours (increasing in 20 pct increments from top), and (*c*) normalized mixture concentration pattern of Ti.

A. *Cases 1 through 4—Original CMSX2*

No figures are shown for Case 1, because all velocities at all times were predicted to be zero within numerical accuracy. In other words, the system is convectively stable. Consequently, the mixture concentrations are uniform and equal to the initial values, because macrosegregation does not exist without flow. Several stability analyses have been performed to predict the onset of convection in directional solidification from below.[16,17,18] Sometimes, critical thermal and/or solutal Rayleigh numbers can be defined below which the system is stable. However, these analyses often use highly simplifying assumptions and are not applicable to the present multicomponent alloy and transient conditions (due to a finite system length). Therefore, no attempt was made to compare the present results to these analyses.

Many preliminary simulations were performed where the temperature gradient (G) and casting speed (R) were varied, in order to detect the conditions that correspond to the onset of convection. It was found that the product $GR = \dot{T}$, *i.e.*, the cooling rate, is the most critical parameter (for a given composition) in determining the onset of convection. We believe that this is due to the fact that in the present model, the cooling rate determines the primary dendrite arm spacing (Table II), and the primary spacing in turn has a strong influence on the mushy zone permeability. The permeability increases with increasing λ_1, and, hence, decreasing cooling rate. A higher permeability provides less resistance to flow in the mush, making the system less stable. By systematically decreasing the cooling rate in steps of about 50 K/h close to the onset, Case 2, with a cooling rate of 350 K/h, was found to be the first instance where convection was predicted. This case corresponds to a primary dendrite arm spacing of 320 μm, whereas Case 1 has $\lambda_1 =$ 210 μm (Table III).

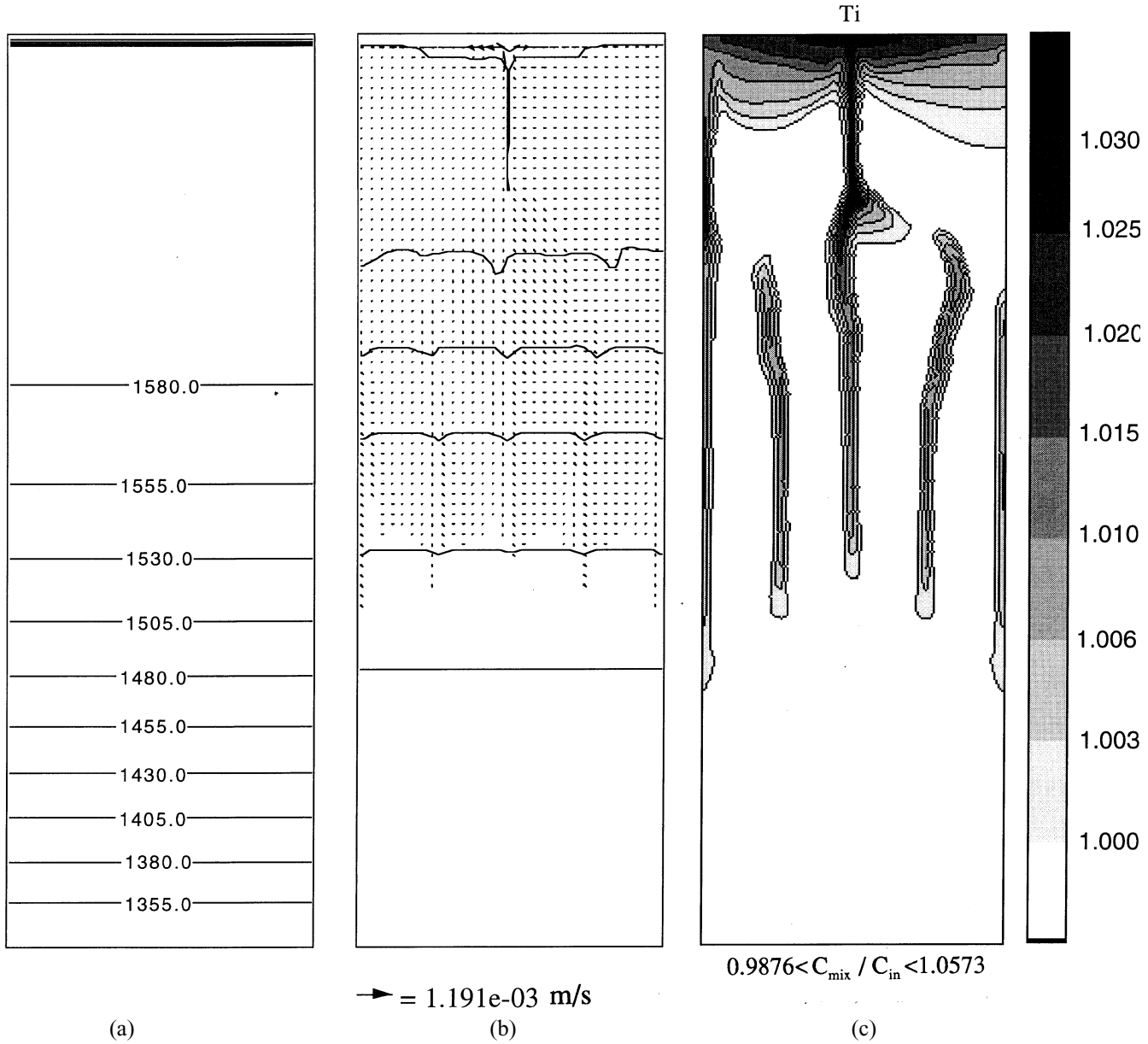

Fig. 7—Case 2 at 4381 s: (*a*) isotherms in Kelvin, (*b*) velocity vectors and solid fraction contours (increasing in 20 pct increments from top), and (*c*) normalized mixture concentration pattern of Ti.

Representative results for Case 2 are shown in Figures 5 through 7 at various times. Figure 5 shows the results close to the onset of convection, 2971 seconds into the simulation. Until about 2500 seconds the system is still convectively stable. The delay can be attributed to initial transients. Convection exists above the mushy zone (*i.e.*, the liquidus isotherm) in the form of six rotating cells, and also penetrates into the high liquid fraction, upper mushy zone. In the upward-flowing regions, solute rich (for $\kappa^m < 1$, or solute poor for $\kappa^m > 1$), lighter liquid is advected out of the mush and rises into the bulk melt in the form of fingers, or solutal plumes. The fingers retain their composition but not their temperature, because of the high value of the Lewis number (*i.e.*, the ratio of the thermal to the mass diffusivity), which is the primary reason for such a double-diffusive convection phenomenon. The maximum melt velocity in the solutal plumes is of the order of 1 mm/s. This value, as well as the somewhat higher ones in the subsequent cases (up to about 7 mm/s in Case 4m, as subsequently discussed), is of the same order of magnitude as the maximum velocities measured by Hellawell *et al.*[5] in their experiments with transparent model alloys. Hellawell *et al.* also provided a theoretical estimate of 140 mm/s for the corresponding velocity in a Pb-Sn metallic alloy (for the same plume diameter). The flow rate in a solutal plume is a function of the buoyancy forces in the melt and the permeability of the mush that feeds the plume. The velocity in such plumes has never been measured for metallic systems. It is unlikely that the mush in the present simulations is sufficiently permeable to sustain the high flow rates estimated by Hellawell *et al.* for their metallic system, and the present predictions appear realistic. Because of the relatively low velocities and high thermal diffusivity, the melt temperature is virtually uniform in the horizontal direction across the plume (Figure 5(a)).

Initially (Figure 5), there exist two fingers in the center

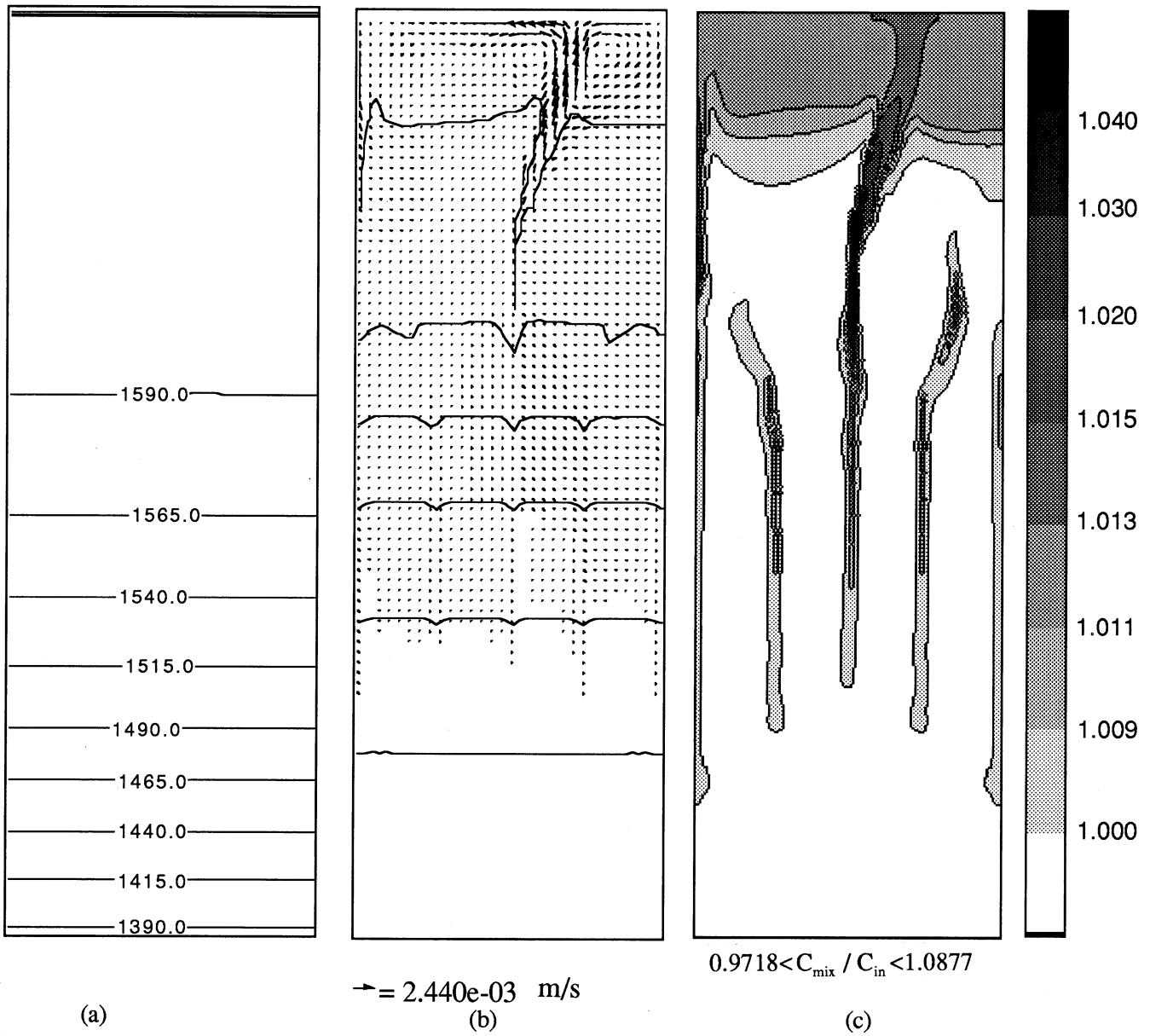

Fig. 8—Case 3 at 4429 s: (*a*) isotherms in Kelvin, (*b*) velocity vectors and solid fraction contours (increasing in 20 pct increments from top), and (*c*) normalized mixture concentration pattern of Ti.

portion of the cavity, about 2.5 cm apart, and two fingers along the vertical sidewalls. A little later, a fifth finger develops in the center of the cavity, as can be seen in Figure 6 at 3451 seconds. The convection now is stronger, the macrosegregation is more pronounced, and small depressions can be seen in the solid fraction contours at the locations of the fingers. The convection and finger patterns continue to evolve, because a true steady state is never achieved in the present case. A longer domain height was not possible due to limited computational resources. At 4381 seconds, the mushy zone has reached the top of the cavity. As can be seen in Figure 7, only two fingers have survived at this time: one at the center and one at the left sidewall, with the center one dominating the convective flow. At the transition point between five and two fingers, the fingers become somewhat curved, which is simply an indication of the changing convection pattern. The mushy zone is now deeply eroded at the location of the center finger, and a solid-free, narrow channel is formed. It is difficult to define an exact width of the channels in the mush, but based on the concentration plots, it is about 3 mm, which corresponds to nine primary dendrite arm spacings in Case 2. The channel widths and spacings predicted in Case 2, as well as in the subsequent cases, are of the same order of magnitude as the measurements of Hellawell and co-workers.[4,5]

Obviously, the predicted macrosegregation pattern will persist in the fully solidified cavity, and the channels become freckle chains. The onset of convection, and therefore the occurrence of freckle chains, is found to be strongly related to the primary dendrite arm spacing. For the present CMSX2 alloy, the critical spacing is between 300 and 320 μm. This number corresponds almost exactly to the experimental value obtained by Pollock and Murphy (Figure 12 in Reference 11). The composition of their SX-1 alloy is somewhat different from the CMSX2 alloy (*i.e.*, it has in-

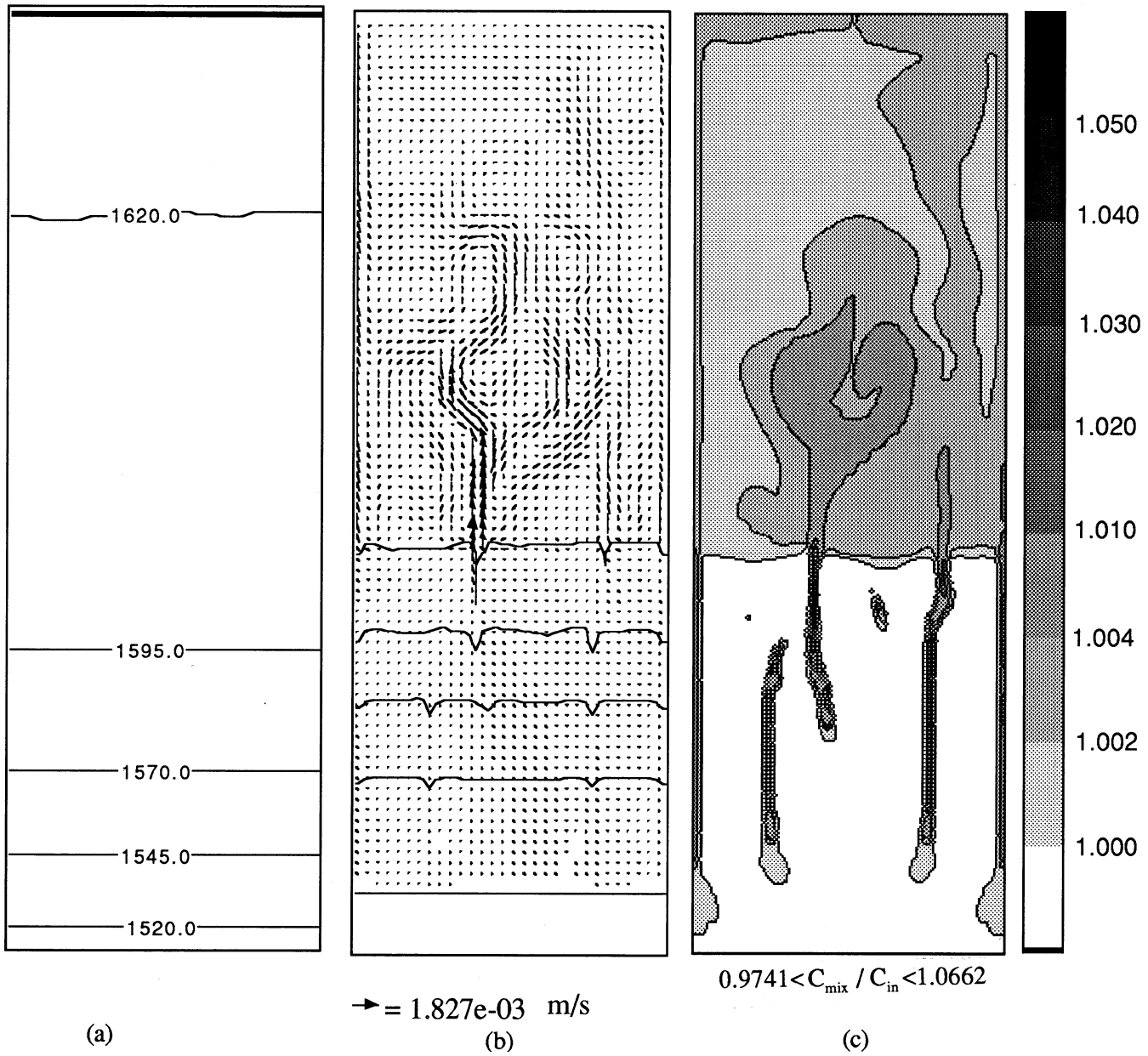

Fig. 9—Case 4 at 4381 s: (*a*) isotherms in Kelvin, (*b*) velocity vectors and solid fraction contours (increasing in 20 pct increments from top), and (*c*) normalized mixture concentration pattern of Ti.

creased contents of both stabilizing and destabilizing elements), but it was estimated that the total density variation of the liquid during solidification of the SX-1 alloy is quite similar to the present one (Figure 3). The good correspondence in freckle occurrence exists despite the fact that the Bridgman-type furnace and sample dimensions in the experiments of Pollock and Murphy[11] are different from the present idealized (2-D) system. This indicates that the onset of convection and freckling may not depend strongly on the mold geometry, and simulations such as the present ones can provide realistic predictions of the onset. The dependence on alloy composition is examined in more detail in section B.

The effect of a slightly lower cooling rate (300 K/h, λ_1 = 340 μm) is investigated in Case 3. The predicted results when the dendrite tips are close to the top boundary (4429 seconds) are shown in Figure 8. Overall, the macrosegregation pattern is very similar to Case 2. However, due to the lower imposed thermal gradient, the onset of convection occurs earlier, and the channels start forming about 2 cm lower in the cavity than in Case 2. In addition, both the melt velocities and the extent of macrosegregation are higher. More pronounced solid-free channels can be observed in the center and along the left sidewall, while the right surface freckle disappears, as in Case 2.

A much lower cooling rate of 200 K/h (or lower imposed temperature gradient) is used in Case 4. The corresponding primary dendrite arm spacing is 400 μm. Predicted isotherms, solid fraction contours, velocities, and macrosegregation patterns are shown in Figures 9 and 10 at two different times. As can be inferred from Figure 9, the onset of convection occurs close to the beginning of the simulation, and channels start forming almost at the bottom of the cavity. Again, a competition takes place between the chan-

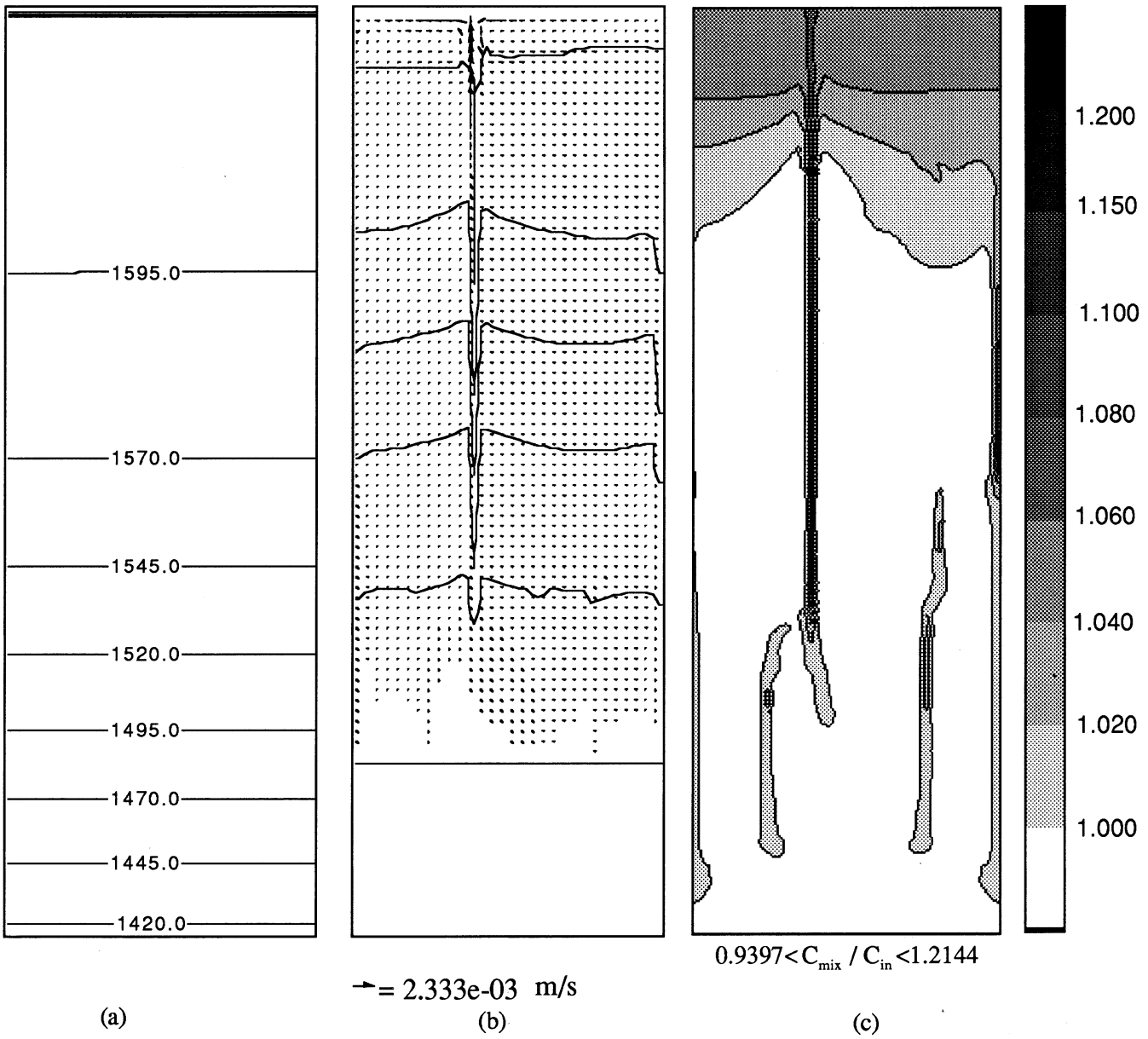

Fig. 10—Case 4 at 6121 s: (*a*) isotherms in Kelvin, (*b*) velocity vectors and solid fraction contours (increasing in 20 pct increments from top), and (*c*) normalized mixture concentration pattern of Ti.

nels in the center portion and at the sidewalls during the initial development of the mushy zone, and at about midheight, as can be seen in Figure 10, only one channel close to the center and one at the right sidewall survive. The one at the right sidewall eventually disappears as well. Because of the lower thermal gradient, the mushy zone is much wider than in the previous cases. One immediate consequence is that the channels in the mush are much longer, which is particularly pronounced in Figure 10. In this figure, the only remaining channel is fed by solute rich (for $\kappa^m < 1$) liquid flowing toward the channel over almost the entire mushy zone height. The solid fraction contours are bent upward near the channel, indicating a volcanolike mush structure. In Case 4, the channel width corresponds to only about five primary dendrite arm spacings. The lower thermal gradient also causes much higher melt velocities and, therefore, stronger macrosegregation. In Figure 10, the maximum positive macrosegregation for Ti (in the freckles) is more than 20 pct, whereas the corresponding value in Case 2 is only 5.7 pct. Despite the higher velocities, the plotted isotherms are still horizontal, indicating unidirectional heat transfer. All convection is driven by solutal buoyancy forces.

B. *Cases 1m and 4m—Modified CMSX2*

Additional simulations were conducted to investigate the effect of alloy composition on the occurrence and nature of channel segregates in the present system. As already mentioned, in the modified CMSX2 alloy, the Ta content was decreased from 6 to 1 pct, while the W content was increased from 8 to 13 pct, making the alloy much more solutally unstable than the original CMSX2.

As before, several simulations were conducted to detect

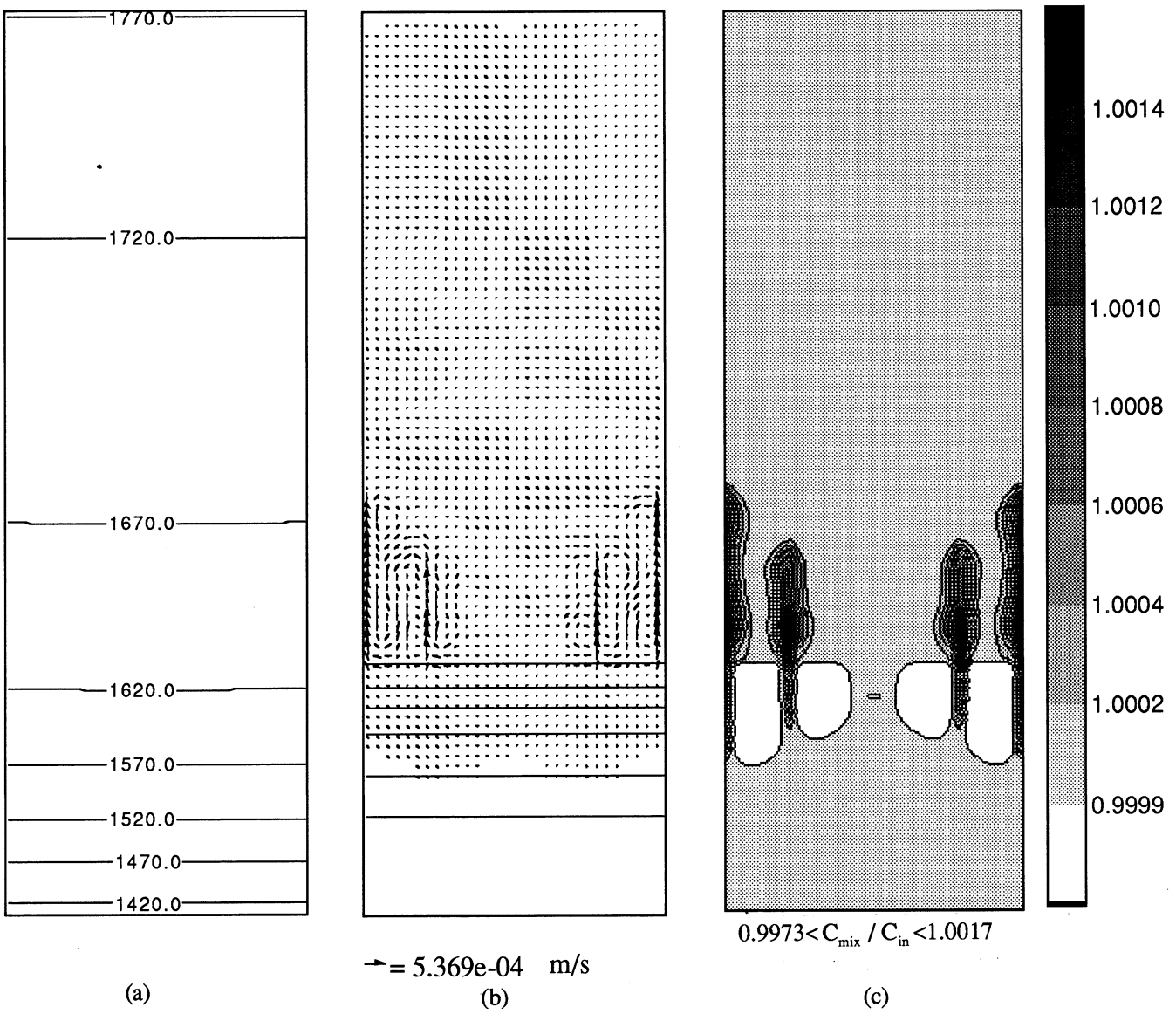

Fig. 11—Case 1m at 1060 s: (*a*) isotherms in Kelvin, (*b*) velocity vectors and solid fraction contours (increasing in 20 pct increments from top), and (*c*) normalized mixture concentration pattern of Ti.

the onset of convection. Case 1m, which features the same casting conditions as Case 1, represents the instance with the highest cooling rate (1250 K/h) where convection was first observed. The onset of convection in this case is illustrated in Figure 11. The cooling rate in Case 1m gives a primary dendrite arm spacing of 210 μm, which is about 100 μm less than the arm spacing at which the onset of convection occurred in the original CMSX2 alloy (Case 2, Figure 5). Consequently, the mushy zone in Case 1m is much less permeable. As in Case 2, however, the initial convection pattern consists of four fingers that are rising out of the mushy zone (Figure 11). Because of the high imposed temperature gradient in Case 1m, the mushy zone is very narrow, and the large casting speed makes it move up quickly. Although no results at a later time are presented here, the extent of macrosegregation was found to remain very low (less than 1 pct Ti).

The effect of the modified alloy composition on the convection and macrosegregation patterns at a much lower cooling rate (200 K/h) is examined in Case 4m. For illustration purposes, only results at an intermediate time (5040 seconds) are shown (Figure 12). In comparison to Case 4 (Figures 9 and 10), the convection velocities are more than three times higher; the channels start forming closer to the bottom; the competition between the channels/fingers terminates earlier; the channels in the mush are deeper and more narrow (less than four λ_1); and the extent of macrosegregation is about twice as high. All of these conditions can be attributed to the stronger solutal buoyancy forces in Case 4m.

V. CONCLUSIONS

A phase equilibrium subroutine has been successfully linked to a previously developed model of heat transfer, melt convection, and micro- and macrosegregation in columnar dendritic solidification, and the combined code has

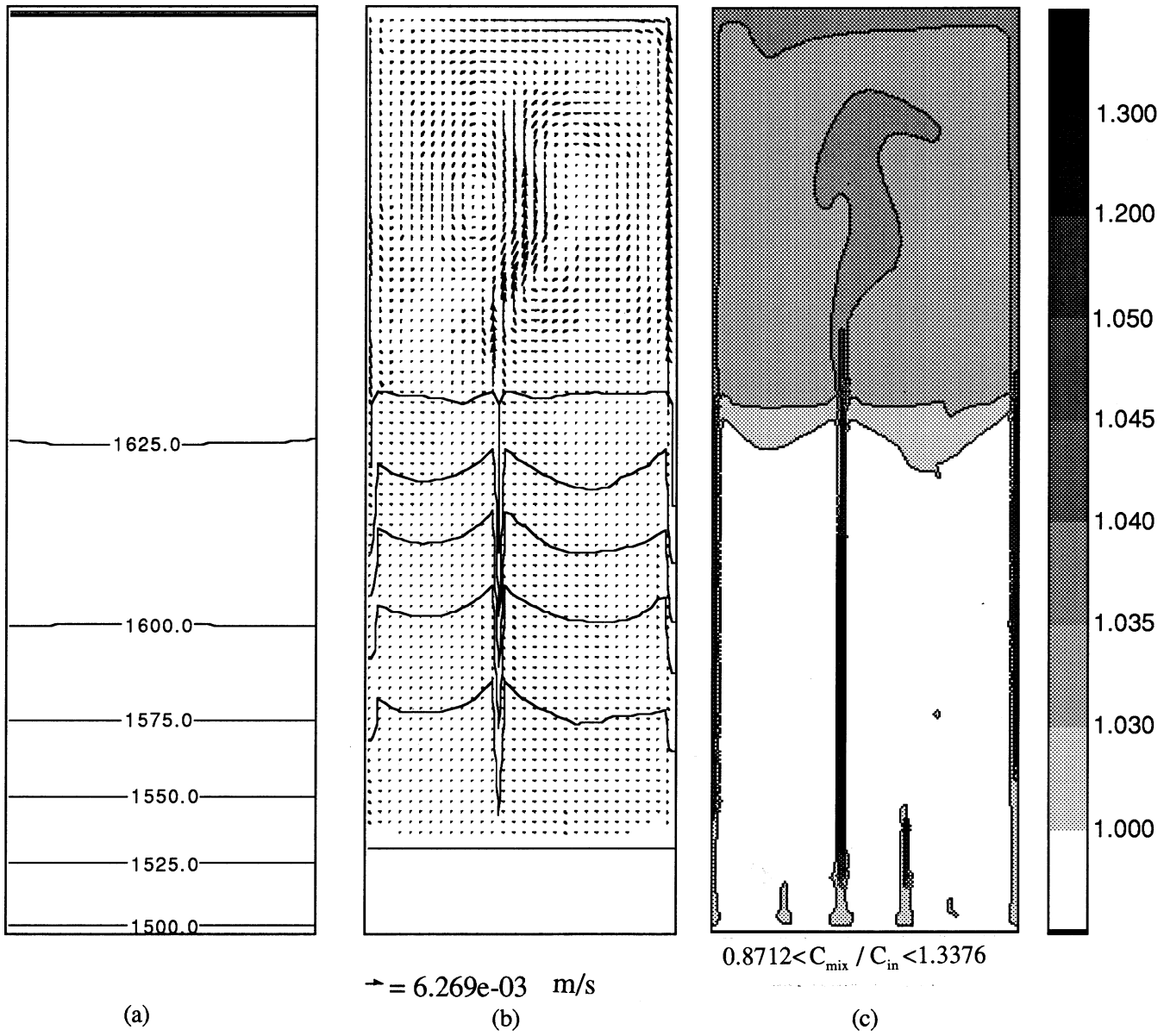

Fig. 12—Case 4m at 5040 s: (*a*) isotherms in Kelvin, (*b*) velocity vectors and solid fraction contours (increasing in 20 pct increments from top), and (*c*) normalized mixture concentration pattern of Ti.

been applied to study the directional solidification of multicomponent single-crystal Ni-base superalloys in a 2-D rectangular domain. With regard to the basic model implementation, the following conclusions can be made.

1. Although no major problems were encountered in linking the general-purpose phase equilibrium subroutine to the solidification code, computational times can become excessive, and special procedures had to be used to limit the number of calls to the subroutine.
2. The present approximate back-diffusion model works well in predicting microsegregation during primary solidification, and the importance of the use of a phase equilibrium subroutine has been demonstrated.
3. Solidification had to be terminated in an isothermal eutectic reaction, and future work should include the extension of the equilibrium calculations to multiple phases in order to predict their occurrence and provide more accurate final solidification paths and temperatures.
4. There exist some uncertainties in the thermophysical properties, especially for the concentration dependence of the liquid density, the thermodynamic database, as well as in the relation used for the mush permeability. With regard to the latter, one improvement could be the use of an anisotropic permeability.[42]
5. Although the present computational grid allows for reasonably realistic predictions, the accuracy of the solutions could be improved by using a finer grid and/or higher-order discretization schemes.

The results of six different directional solidification simulations were presented, and they allow for the following conclusions.

1. The onset of convection coincides with the occurrence of channels and freckle defects and depends primarily on the primary dendrite arm spacing and, hence, the imposed cooling rate.
2. The critical primary dendrite arm spacing corresponding

to the onset in the original CMSX2 alloy (~320 μm) agrees well with the experimental value of Pollock and Murphy[11] for an alloy that has a similar variation in the liquid density during solidification. For the more unstable modified CMSX2 alloy, the critical value is, as expected, much lower.

3. In the unstable cases, the simulations provide a detailed picture of the evolution of the convection and macrosegregation patterns for a variety of casting conditions and two alloy compositions. The results indicate a competition between channels due to transients and the simultaneous occurrence of surface and bulk channel segregates.
4. The development and nature of the channel segregates (mush structure, flow patterns, length, width, and spacing) qualitatively agree with previous experimental observations.[3,4,5] Nonetheless, it should be kept in mind that freckling is inherently a three-dimensional phenomenon.

Further work will include the application of the present model to more practically relevant geometries and thermal conditions. From a more fundamental point of view, it would be interesting to extend the model to include dendrite tip undercooling, more detailed accounting of remelting, and also the complete breakdown of the columnar structure into an equiaxed one.[11] A companion article[43] describes a model and preliminary calculations for the transport and partial remelting of dendrite fragments originating in the channels and potentially leading to spurious grains.

NOMENCLATURE

C	concentration (wt pct)
c	specific heat (J/kg/K)
D	diffusion coefficient (m^2/s)
G	temperature gradient (K/cm)
H	height of the system (m)
T	temperature (K)
$\dot{T}$	cooling rate (K/h)
K	permeability (m^2)
k	thermal conductivity (W/m/K)
L	latent heat (J/kg)
m	liquidus slope (K/wt pct)
Q	activation energy (J/mol)
R	casting speed (cm/h)
$\bar{R}$	universal gas constant (J/mol/K)

Greek Symbols

β_C	solutal expansion coefficient (wt pct^{-1})
β_T	thermal expansion coefficient (K^{-1})
ε	volume fraction (−)
κ	partition coefficient (−)
λ_1	primary dendrite arm spacing (μm)
λ_2	secondary dendrite arm spacing (μm)
μ	dynamic viscosity (kg/m/s)
ρ	density (kg/m^3)

Subscripts

c	cold (bottom) wall
h	hot (top) wall
in	initial
l	liquid
mix	mixture
ref	reference
s	solid

Superscripts

m	species m

ACKNOWLEDGMENTS

This work was supported in part by the Advanced Research Project Agency, under the Micromodeling program of the Investment Casting Cooperative Arrangement (ICCA), through a subcontract to Howmet Corporation (Dr. Boyd Mueller, technical contact), and by the National Science Foundation, under Grant No. CTS-9501389. Computer facilities were made available by NIST. The authors thank A.F. Giamei, UTRC, and other members of the ICCA consortium for fruitful discussions.

REFERENCES

1. A.F. Giamei and B.H. Kear: *Metall. Trans.*, 1970, vol. 1, pp. 2185-92.
2. S.M. Copley, A.F. Giamei, S.M. Johnson, and M.F. Hornbecker: *Metall. Trans.*, 1970, vol. 1, pp. 2193-2204.
3. N. Streat and F. Weinberg: *Metall. Trans.*, 1974, vol. 5, pp. 2539-48.
4. A.K. Sample and A. Hellawell: *Metall. Trans. A*, 1984, vol. 15A, pp. 2163-73.
5. A. Hellawell, J.R. Sarazin, and R.S. Steube: *Phil. Trans. R. Soc. London A*, 1993, vol. 345, pp. 507-44.
6. K.O. Yu, M.J. Beffel, M. Robinson, D.D. Goettsch, B.G. Thomas, D. Pinella, and R.G. Carlson: *AFS Trans.*, 1990, vol. 98, pp. 417-28.
7. K.O. Yu, J.J. Nichols, and M. Robinson: *JOM*, 1992, vol. 44, pp. 21-25.
8. J.S. Tu and R.K. Foran: *JOM*, 1992, vol. 44, pp. 26-28.
9. A.L. Purvis, C.R. Hanslits, and R.S. Diehm: *JOM*, 1994, vol. 46, pp. 38-41.
10. A.L. Purvis, C.R. Hanslits, and R.S. Diehm: *AFS Trans.*, 1994, vol. 102, pp. 637-44.
11. T.M. Pollock and W.H. Murphy: *Metall. Mater. Trans. A*, 1996, vol. 27A, pp. 1081-94.
12. M.C. Flemings and G.E. Nereo: *TMS-AIME*, 1967, vol. 239, pp. 1449-61.
13. D.G. Neilson and F.P. Incropera: *Int. J. Heat Mass Transfer*, 1993, vol. 36, pp. 489-503.
14. S.D. Felicelli, F.C. Heinrich, and D.R. Poirier: *Metall. Trans. B*, 1991, vol. 22B, pp. 847-59.
15. H. Combeau and G. Lesoult: in *Modeling of Casting, Welding and Advanced Solidification Process VI*, T.S. Piwonka, V. Voller, and L. Katgerman, eds., TMS, Warrendale, PA, 1993, pp. 201-08.
16. A.C. Fowler: *IMA J. Appl. Math.*, 1985, vol. 35, pp. 159-74.
17. P. Nandapurkar, D.R. Poirier, J.C. Heinrich, and S. Felicelli: *Metall. Trans. B*, 1989, vol. 20B, pp. 711-21.
18. M.G. Worster: *J. Fluid Mech.*, 1992, vol. 237, pp. 649-69.
19. F. Roch, H. Combeau, I. Poitrault, J.Ch. Chevrier, and G. Lesoult: *Proc. 6th Int. Iron and Steel Congr., Vol. 1: Fundamental*, Iron and Steel Institute of Japan, Nagoya, Japan, 1990, pp. 665-72.
20. H. Combeau, F. Roch, I. Poitrault, J.Ch. Chevrier, and G. Lesoult: *Advanced Computational Methods in Heat Transfer, Vol. 3: Phase Change and Combustion Simulation*, Springer-Verlag, New York, NY, 1990, pp. 79-90.
21. H. Combeau, F. Roch, I. Poitrault, J.Ch. Chevrier, and G. Lesoult: *Modeling of Casting, Welding and Advanced Solidification Process V*, TMS, Warrendale, PA, pp. 789-95.
22. H. Vannier, H. Combeau, and G. Lesoult: *Numerical Methods in Industrial Forming Process*, A.A. Balkema, Rotterdam, The Netherlands, 1992, pp. 835-40.
23. M.C. Schneider and C. Beckermann: *Metall. Mater. Trans. A*, 1995, vol. 26A, pp. 2373-88.
24. W.D. Cao, R.L. Kennedy, and M.P. Willis: in *Superalloys 718, 625 and Various Derivatives*, E.A. Loria, ed., TMS, Warrendale, PA, 1991, pp. 147-59.
25. R.G. Thompson, D.E. Mayo, and B. Radhahrishnan: *Metall. Trans. A*, 1991, vol. 22A, pp. 557-67.

26. G.A. Konorovsky, M.J. Cieslka, T.J. Headly, A.D. Roming, and W.F. Hammetter: *Metall. Trans. A*, 1989, vol. 20A, pp. 2149-58.
27. B. Radhakrishnan and R.G. Thompson: *Metall. Trans. A*, 1989, vol. 20A, pp. 2866-68.
28. B. Radhakrishnan and R.G. Thompson: *Metall. Trans. A*, 1991, vol. 22A, pp. 887-902.
29. J. Zou, H.P. Wang, R. Doherty, and E.M. Perry: in *Superalloys 1992*, S.D. Antolovich, R.W. Stusrud, R.A. MacKay, D.L. Anton, T. Khan, R.D. Kissinger, and D.L. Klarstrom, eds., TMS, Warrendale, PA, 1992, pp. 165-74.
30. L. Nastac and D.M. Stefanescu: *Metall. Trans. A.*, 1993, vol. 24A, pp. 2107-18.
31. H.P. Wang, J. Zou, E.M. Perry, L.R. Kaisand, and R. Dohety: in *Modeling of Casting, Welding and Advanced Solidification Process VI*, T.S. Piwonka, V. Voller, and L. Katgerman, eds., TMS, Warrendale, PA, 1993, pp. 45-52.
32. W.J. Boettinger, U.R. Kattner, S.R. Coriell, Y.A. Chang, and B.A. Mueller: in *Modeling of Casting, Welding and Advanced Solidification Process VII*, M. Cross and J. Campbell, eds., Warrendale, PA, 1995, pp. 649-56.
33. U.R. Kattner, W.J. Boettinger, and S.R. Coriell: *Z. Metallkd.*, 1996, vol. 87, pp. 522-28.
34. C.Y. Wang and C. Beckermann: *Metall. Trans. A*, 1993, vol. 24A, pp. 2787-2802.
35. T.G. Chart, J.F. Counsell, W. Slough, and P.J. Spencer: *Int. Met. Rev.*, 1975, vol. 20, p. 57.
36. T. Iida and R.I.L. Guthrie: in *The Physical Properties of Liquid Metals*, Clarendon Press, Oxford, United Kingdom, 1993, pp. 70-73.
37. M.C. Bhat: Ph.D. Thesis, The University of Arizona, Tucson, AR, 1995.
38. P.N. Quested and M. McLean: *Mater. Sci. Eng.*, 1984, vol. 65, pp. 171-84.
39. G.K. Bouse and J.R. Mihalisin: in *Superalloys, Supercomposites and Superceramics*, J.K. Tien and T. Caulfield, eds., Academic Press, Boston, MA, 1988, pp. 99-148.
40. B. Mueller: Howmet Corporation, Whitehall, MI, personal communication, 1995.
41. M.C. Schneider: Ph.D. Thesis, The University of Iowa, Iowa City, IA, 1995.
42. M.C. Schneider and C. Beckermann: *Int. J. Heat Mass Transfer*, 1995, vol. 38, pp. 3455-73.
43. J.P. Gu, C. Beckermann, and A.F. Giamei: *Metall. Mater. Trans. A*, 1997, vol. 28A, pp. 1533-42.